CHEMISTRY OF MATERIALS

Article

pubs.acs.org/cm

Understanding Phase Transformation in Crystalline Ge Anodes for Li-Ion Batteries

Linda Y. Lim,[†,‡] Nian Liu,[§] Yi Cui,[†] and Michael F. Toney*[,‡]

[†]Department of Materials Science and Engineering and [§]Department of Chemistry, Stanford University, Stanford, California 94305, United States

[‡]Stanford Synchrotron Radiation Lightsource, SLAC National Accelerator Laboratory, Menlo Park, California 94025, United States

Supporting Information

ABSTRACT: Lithium-ion batteries using germanium as the anode material are attracting attention because of their high-capacity, higher conductivity, and lithium-ion diffusivity relative to silicon. Despite recent studies on Ge electrode reactions, there is still limited understanding of the reaction mechanisms governing crystalline Ge and the transformations into intermediate amorphous phases that form during the electrochemical charge and discharge process. In this work, we carry out in operando X-ray diffraction (XRD) and X-ray absorption spectroscopy (XAS) studies on Ge anodes during the initial cycles to better understand these processes. These two probes track both crystalline (XRD) and amorphous (XAS) phase transformations with potential, which allows detailed information on the Ge anode to be obtained. We find that crystalline Ge lithiates inhomogeneously, first forming amorphous Li_9Ge_4 during the beginning stage of lithiation, followed by the conversion of the remaining crystalline Ge to amorphous Ge. The lithiation of amorphous Ge then forms amorphous Li_xGe, which are then further lithiated to form crystalline $Li_{15}Ge_4$. During delithiation, crystalline $Li_{15}Ge_4$ transforms directly into a heterogeneous mix of amorphous Li_xGe, which eventually form amorphous Ge, and interestingly, no amorphous Li_9Ge_4 are detected. Both our in operando XRD and XAS results present new insights into the reaction mechanism of Ge as anodes in LIBs, and demonstrate the importance of correlating electrochemical results with in operando studies.

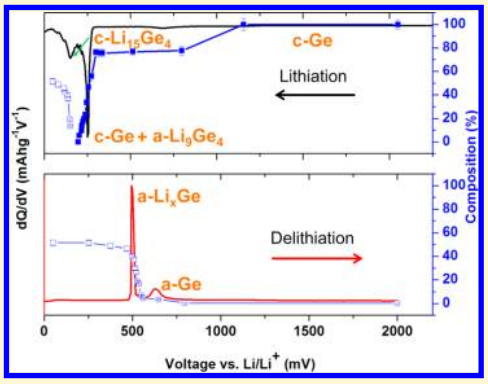

1. INTRODUCTION

One of the most important renewable energy storage technologies is lithium-ion batteries (LIBs).[1−3] The emerging market for plug-in hybrid and electric vehicles requires lightweight, safe, durable, and high-capacity rechargeable LIBs.[4,5] Additionally, the global increase of portable consumer electronics as well as electric vehicles further demands rechargeable batteries with high capacity and short charging time.[6,7] However, current LIB materials do not meet the growing demand for these applications partly because of capacity limitations. Among the potential alternative anode materials, group 14 elements, such as silicon (Si) and germanium (Ge), are very attractive candidates for high-capacity applications as they possess high theoretical capacities (3850 mA h g^{-1} for Si, 1568 mA h g^{-1} for Ge), because of their ability to alloy with as many as 4.4 Li atoms per Si or Ge atom.[8] In particular, Ge is a promising candidate for fast-charging and high-capacity LIBs applications, with lithium diffusivity in Ge being 400 times higher than in Si,[9] and higher intrinsic electronic conductivity compared to Si due to its smaller band gap.[10]

There are many reports which focus on improving the active anode material[10−16] for LIBs, but relatively fewer studies on the mechanisms and phase transformations that occur during battery cycling.[17−20] To guide the design of a better electrode, however, a more complete understanding of its reaction mechanism is required. Though there has been recent progress in understanding the reaction mechanism in Ge electrodes, these were largely limited to ex situ studies, which suffer from possible artifacts.[17,18] Additionally, most of the ex situ studies on Ge electrodes presented different findings on the Li−Ge phases formed and the presence (or absence) of crystalline Ge at the end of the delithiation cycle. Yoon et al. carried out ex situ X-ray diffraction (XRD) of Ge and carbon-coated Ge composites micrometer particles cycled at a constant current of 100 mA g^{-1} and reported that crystalline Li_9Ge_4 and Li_7Ge_2 were observed as intermediate phases, while both $Li_{15}Ge_4$ and $Li_{22}Ge_5$ were observed together at the end of lithiation, and no Ge crystalline peak was observed at the end of delithiation.[18] Similarly, no crystalline Ge peak and crystalline Li−Ge phases were observed at the end of delithiation of single-crystal Ge nanowires cycled at a rate of C/20 in an ex situ study.[21] On the other hand, Graetz et al. observed crystalline peaks of Li−Ge phases upon lithiation of evaporated amorphous Ge thin film cycled at a rate of C/4 in ex situ XRD studies, and a strong Ge (111) diffraction peak was observed upon delithiation.[17] Recent

Received: April 7, 2014
Revised: May 16, 2014

   dx.doi.org/10.1021/cm501233k | Chem. Mater. XXXX, XXX, XXX−XXX

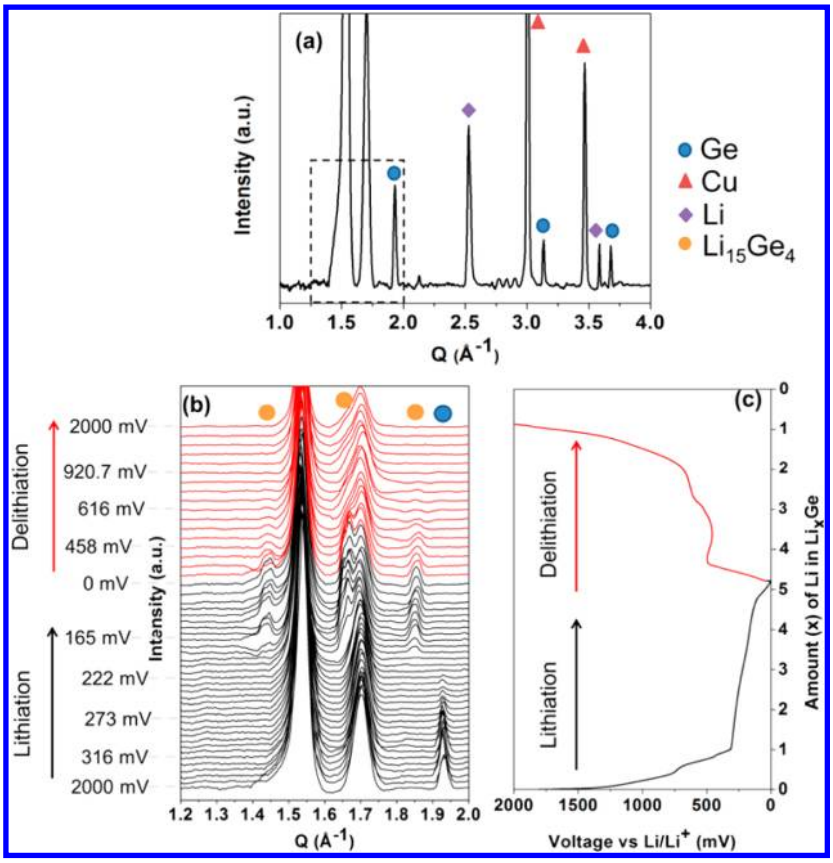

Figure 1. In operando XRD results for a GeMP cell cycled at C/15. (a) XRD pattern before the first cycle. (b) Real-time XRD patterns showing the magnified portion in (a) for the first cycle. Unlabeled XRD peaks are associated with either the polyester pouch or polymer separator. (c) Corresponding electrochemical voltage profile (lithiation in black and delithiation in red). The cell was cycled at a rate of C/15.

reports on in situ X-ray studies of Ge electrodes enable us to further understand the reaction mechanism in Ge electrodes during electrochemical cycling.[19,20] An in situ XRD study of amorphous Ge thin films cycled at a rate of C/20 revealed the observation of only $Li_{15}Ge_4$ at the end of lithiation,[19] whereas from in situ X-ray absorption spectroscopy (XAS) of amorphous Ge thin films cycled at a rate of C/20, it was postulated that the lithiation for amorphous Ge thin films proceeded with the formation of amorphous LiGe followed by amorphous Li_7Ge_2 and finally crystalline $Li_{15}Ge_4$ at the end of lithiation.[20] It is clear that there are apparent discrepancies between the results obtained from ex situ and in situ studies, as well as an apparent dependence on different starting morphologies and rate of electrochemical cycling of the Ge electrodes.

In this work, we choose to study crystalline micrometer Ge particles in operando because these have a similar morphology to practical battery electrode materials without postprocessing of the electrode materials. To the best of our knowledge, there have been no reports on in operando X-ray studies on micrometer-sized crystalline Ge particles as LIB anodes.

Using synchrotron-based, in operando XRD and XAS, and by correlating these structural studies with electrochemical cycling data, we are able to track the crystalline and amorphous phases that form during electrochemical cycling. Such understanding would enable us to further improve on the performance of Ge and Ge-based materials as anodes for LIBs. From our in operando XRD results, we observe disappearance of crystalline Ge and the appearance of $Li_{15}Ge_4$ diffraction peaks near the end of the initial lithiation; we observe no diffraction peaks belonging to other Li−Ge phases. In operando XAS shows evidence that crystalline Ge initially forms an amorphous phase with local structure resembling Li_9Ge_4 as well as some amorphous Ge. As lithiation proceeds, the amorphous Ge transforms into an amorphous heterogeneous mix of Li_xGe alloys, and finally crystalline $Li_{15}Ge_4$. During delithiation, crystalline $Li_{15}Ge_4$ transforms into an amorphous phase resembling a heterogeneous mix of Li_xGe before the formation of amorphous Ge. Interestingly, we do not observe any evidence of local structure resembling amorphous Li_9Ge_4 during delithiation. Both our XRD and XAS results present new insights into the reaction mechanism of Ge as anodes in LIBs and demonstrate the importance of correlating electrochemical results with in operando studies.

2. EXPERIMENTAL SECTION

2.1. Fabrication of Ge Microparticle (GeMP) Electrodes. To minimize the surface oxides, we ground Ge chips (99.999% metal basis, Sigma-Aldrich) in Ar-filled glovebox to produce Ge powders of particle size ∼1 to ∼10 μm. The freshly produced Ge powders were mixed with carbon black (Super P, TIMCAL, Switzerland) and polyvinylidene difluoride binder (PVDF, Kynar HSV 900) with a mass ratio of 45:45:10 and stirred in *N*-methylpyrrolidone (NMP) overnight. Cu-mesh (copper, 200 mesh, TWP Inc.) was dip-coated with this slurry and baked in a vacuum oven at 90 °C for >3 h before cell assembly. The mass of the GeMPs in a given experiment (ca. 0.2 mg) was determined using a microbalance (Sartorius SE2, 0.1 μg resolution).

2.2. In Operando XRD/XAS Cells and Electrochemistry. The in operando battery cells were fabricated out of a GeMP/Cu-mesh electrode, Li metal as the counter electrode and a Celgard separator

dx.doi.org/10.1021/cm501233k | Chem. Mater. XXXX, XXX, XXX−XXX

soaked in electrolyte, similar to previous reports.[22,23] The electrolyte was 1.0 M $LiPF_6$ in 1:1 (w/w) ethylene carbonate:diethyl carbonate (BASF). The cells were assembled inside an Ar-filled glovebox and sealed in 0.11 mm thick transparent polyester pouches (Kapak Corporation). For efficient sealing of the battery cells, pretaped Ni current collectors (MTI Corporation) were used. In operando battery cycling was performed using a MTI eight channel battery analyzer (0.002−1 mA). The voltage cutoffs were typically 2.0 and 0 V vs. Li/Li^+ and the cycling rate was typically $C/15$ in terms of the theoretical capacity of Ge (1568 mA h g^{-1}).

2.3. Synchrotron X-ray Diffraction. In operando XRD measurements were performed at the Stanford Synchrotron Radiation Lightsource (SSRL) beamline 11−3 with a photon wavelength of 0.974 Å. Measurements were done in transmission on pouch cells. The beam size on the sample was 50 μm × 50 μm. The detector was located at a distance of 150 mm from the sample. The scattering intensity was detected on a 2D image plate detector (MAR-345) with a pixel size of 150 μm (2300 × 2300 pixels). To ensure good electrical contact between the current collectors, electrode, and Li metal during X-ray measurements, the pouch cells were sandwiched between two parallel aluminum plates and tightened with screws (see Figure S1 in the Supporting Information). The side of the plate facing the detector has a concave cutoff to allow X-rays with high scattering angles to pass through, which increases the amount of transmitted photons to the detector. Data were collected in 5 min intervals with an exposure time of 200 s. Data were internally calibrated using the copper diffraction peaks and analyzed using WxDiff software package.[24] Background subtraction was done using Origin software package (OriginLab, Northampton, MA).

2.4. Synchrotron X-ray Absorption Spectroscopy. Ge K edge XAS measurements were performed at SSRL beamline 4−1, which is equipped with a double crystal Si (220) monochromator. Harmonic rejection was achieved by detuning the second monochromator crystal so that the intensity of the incident beam was reduced by approximately 35%. Energy calibration was monitored by the use of metallic Ge (11103.0 eV). The XAS spectra were recorded in transmission for the pouch cells in 15 min interval using the same cell setup as in XRD (see Figure S1 in the Supporting Information). Spectra were background-subtracted and normalized using ATHENA software[25] to obtain the extended X-ray absorption fine structure (EXAFS) oscillations. Data were Fourier transformed (FT) in the k range of 3−12 $Å^{-1}$. EXAFS analysis was carried out in the program ARTEMIS.[25] Coordination numbers N, atomic distances R and Debye−Waller factors σ^2 were determined for the first nearest neighbor shell. Each data set was fitted simultaneously with multiple k weightings (1−3) to reduce correlations among the fitting parameters. To further reduce the correlation between N and σ^2, the σ^2 values of Ge−Ge and Ge−Li scattering paths were fixed to 0.005 and 0.01, respectively, which were the average of the σ^2 values for Ge−Ge and Ge−Li paths initially obtained from fitting each data. The amplitude reduction factor S_0^2 value is 0.78 ± 0.06, and was determined by fitting the pristine Ge powder. This value is kept constant in subsequent data fitting.

3. RESULTS AND DISCUSSION

3.1. In Operando X-ray Diffraction. The in operando XRD results of a Ge cell during the first galvanostatic electrochemical cycle, as a function of amount of Li (x, where $0 < x \leq 3.75$) in Li_xGe, are presented in Figure 1. Here, x is likely to be slightly overestimated as some amount of Li also contributes to the formation of the solid electrolyte interphase (SEI) layer. The XRD pattern before cycling is presented in Figure 1a. The labeled diffraction peaks correspond to Ge (Q = 1.92 $Å^{-1}$ (111), 3.14 $Å^{-1}$ (220), and 3.68 $Å^{-1}$ (311)), the Cu mesh (Q = 3.00 $Å^{-1}$ (111) and 3.47 $Å^{-1}$ (200)), and Li foil (Q = 2.55 $Å^{-1}$ (111) and 3.60 $Å^{-1}$ (200)). All other unlabeled peaks are associated with either the polyester pouch or polymer separator. Figure 1b presents a magnified view indicated by a rectangular box in Figure 1a, and Figure 1c shows the corresponding voltage profile as a function of amount of Li (x) in Li_xGe. During lithiation, the intensities of the Ge peaks decrease and disappear completely at ∼210 mV versus Li/Li^+, equivalent to a Li content of x = 3.17. Following this, peaks corresponding to $Li_{15}Ge_4$ (Q = 1.42 $Å^{-1}$ (211), 1.65 $Å^{-1}$ (220), and 1.84 $Å^{-1}$ (310)) emerge at ∼151 mV (x = 4.30) and are present until the end of the lithiation. This contrasts with previous ex situ XRD studies, where Li_9Ge_4 and Li_7Ge_2 were observed as intermediate crystalline phase for Ge electrodes consisting of amorphous thin film[17] and micrometer-size Ge particles.[18] Upon delithiation, the intensities of crystalline $Li_{15}Ge_4$ peaks decrease and disappear at ∼560 mV (x = 3.28). No crystalline Ge peaks are present near the end of the delithiation cycle (Figure 1b), contrary to what was reported in a previous ex situ study of amorphous Ge thin films,[17] where crystalline Ge (111) peak was observed at the end of delithiation cycle. It is worth noting that our observation agrees qualitatively with previous in situ XRD study of amorphous Ge thin film cycled at a rate of $C/20$,[19] where only crystalline $Li_{15}Ge_4$ diffraction peaks were observed at the end of lithiation cycle, and that no crystalline Ge was observed at the end of delithiation. Comparing our work and Refs19 with previous ex situ studies (Refs 17, 18, and 21) largely shows that the starting morphology of the electrode material and cycle rate are less important factors in governing the electrochemical process of Ge electrodes, and instead, postprocessing of Ge electrodes for subsequent ex situ characterization produces artifacts (in this case, crystallization of intermediate Li−Ge phases during lithiation, and crystallization of Ge at the end of delithiation, as demonstrated in Refs 17 and 18), which are otherwise not present during battery operation. The differences between our findings and previous ex situ studies highlight the importance of in situ/in operando studies on energy storage materials in giving a more realistic picture of the electrochemical processes under real time conditions.

To further investigate the phase change behavior, we plotted the crystalline phase fractions from integrating intensities of Ge (111) and $Li_{15}Ge_4$ (310) diffraction peaks in Figure 2 together with the differential capacity curves for lithiation (Figure 2a) and delithiation (Figure 2b). A differential capacity curve is obtained by differentiating the capacity with respect to voltage,

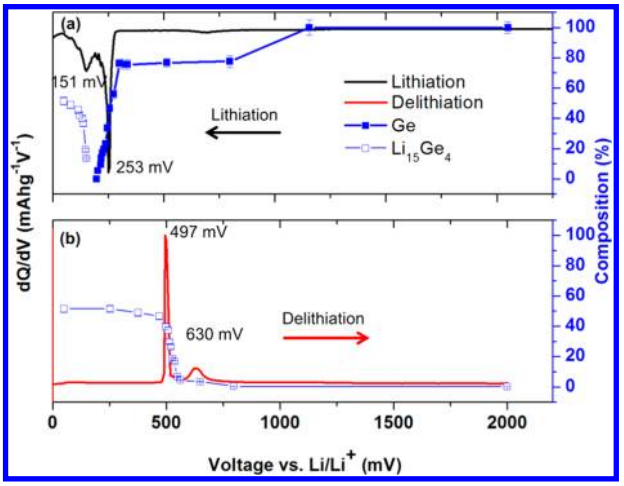

Figure 2. Crystalline phase compositions from Ge (111) and $Li_{15}Ge_4$ (310) XRD peaks and differential capacity plots for (a) lithiation and (b) delithiation.

dx.doi.org/10.1021/cm501233k | Chem. Mater. XXXX, XXX, XXX−XXX

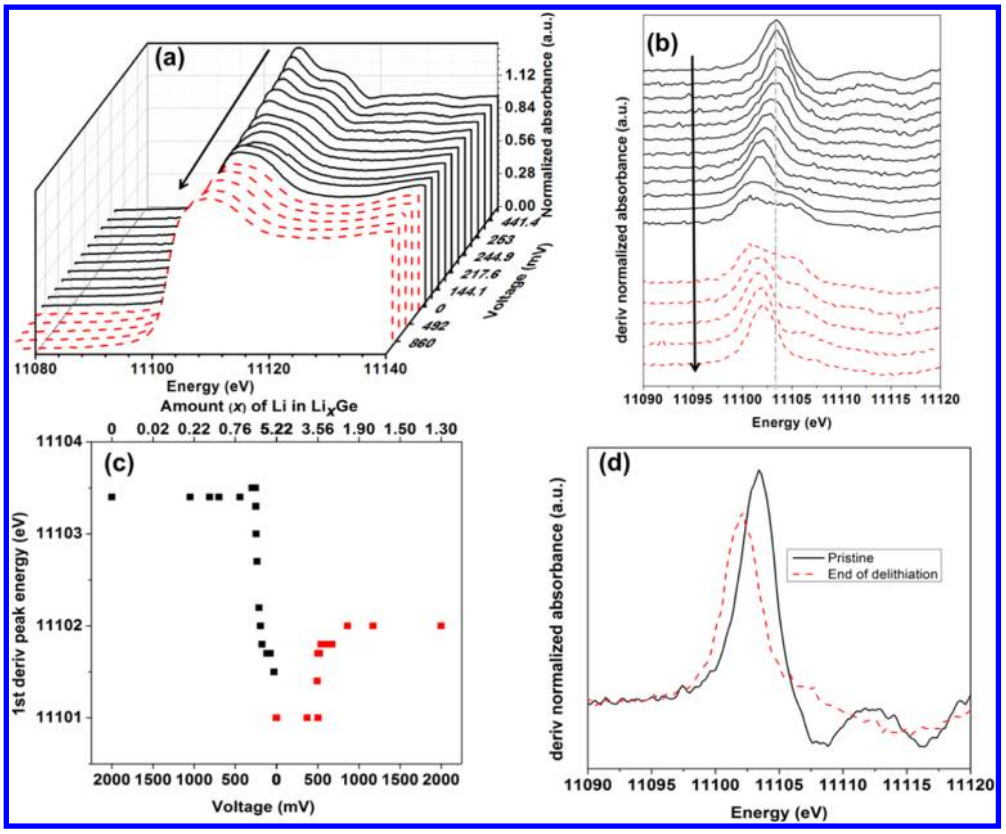

Figure 3. (a) Normalized in operando Ge K-edge XANES spectra for lithiation (black solid) from pristine (x = 0) to V = 0 mV (x = 5.22), and delithiation (red dash) from V = 370 mV (x = 4.91) to V = 2000 mV (x = 1.30). A larger version with the respective voltages and x values for b can be found in Figure S2 in the Supporting Information. (b) Corresponding normalized first derivative of XANES spectra for lithiation (black solid) and delithiation (red dash); the dotted line indicates the peak position for pristine Ge, (c) plot of the first derivative peak energy position as a function of voltage and amount (x) of Li in Li_xGe, and (d) a comparison between the first derivative spectrum before lithiation (black solid) and at the end of delithiation (red dash).

and is useful for evaluating voltage values where phase transformations take place. A peak in the differential capacity indicates phase transformation and coexistence of phases. During lithiation (Figure 2a), the initial slight decrease in the crystalline Ge phase composition occurs below 1155 mV. This could be attributed to both the SEI formation from the reaction between the Ge electrode and the organic electrolyte, as well as the formation of Li^+ interstitials in Ge disrupting crystalline order. Subsequently, the c-Ge (crystalline Ge) phase fraction stays fairly constant until ~253 mV (x = 2.44) where this decreases sharply. This sharp decrease in the c-Ge fraction is the phase transformation taking place at 253 mV with c-Ge reacting with lithium, forming a two-phase region consisting of c-Ge and an unidentified amorphous Li−Ge phase. The c-Ge phase composition reaches zero at ~210 mV (x = 3.33). The emergence of $Li_{15}Ge_4$ (310) diffraction peak takes place at ~151 mV (x = 4.30), coinciding with another broad phase transformation at 151 mV as shown in the differential capacity. The fraction of crystalline $Li_{15}Ge_4$ (c-$Li_{15}Ge_4$) increases quickly and then more slowly until the end of lithiation. It is worth noting that at the end lithiation, only 56% of the original Ge electrode transformed to c-$Li_{15}Ge_4$, which indicates that the lithiation of our micrometer size Ge is an inhomogeneous process, and that the electrode at the end of lithiation consists of c-$Li_{15}Ge_4$ and amorphous Li−Ge (a-Li−Ge).

During delithiation (Figure 2b), the amount of c-$Li_{15}Ge_4$ remains fairly constant until it starts to decrease at ~377 mV (x = 4.90), and subsequently there is a sudden drop at ~497 mV (x = 3.57). The $Li_{15}Ge_4$ (310) peak eventually becomes negligible at about 560 mV (x = 3.28), showing that all the c-$Li_{15}Ge_4$ has transform into a-Li−Ge. Finally, the broad peak in Figure 2b shows another phase transformation occurs at ~630 mV (x = 2.85); however, the phases that form are not clear from the XRD results because no other crystalline phase is observed. It is worth noting that the shape of the differential capacity plot in Ref 17 is quite different compared with the one in our work. This could be attributed to different experimental conditions, namely the starting form of Ge, and the rate at which the electrode is being cycled. First, the form of Ge reported in Ref 17 is ballistically deposited and amorphous evaporated thin films, whereas in this manuscript, we use crystalline GeMPs. Second, the cycling rate used in Ref 17 was about 3 times faster than what we used (C/4 vs C/15), and therefore it is very likely that the electrochemical process in Ref 17 is different from that in our work. Additionally, the second peak in the delithiation process in Ref 17 is much sharper than the first peak, which is a good evidence that recrystallization of Ge had occurred.

3.2. In Operando X-ray Absorption Spectroscopy. To investigate the amorphous phases that are present during the electrochemical cycling, in operando XAS was carried out. The X-ray absorption near-edge structure (XANES) spectra recorded during the galvanostatic electrochemical cycle are presented in Figure 3a. At the start of the lithiation cycle, the white-line of the XANES spectrum is sharp, but becomes broader as lithiation proceeds, with the onset of the broadening

dx.doi.org/10.1021/cm501233k | Chem. Mater. XXXX, XXX, XXX−XXX

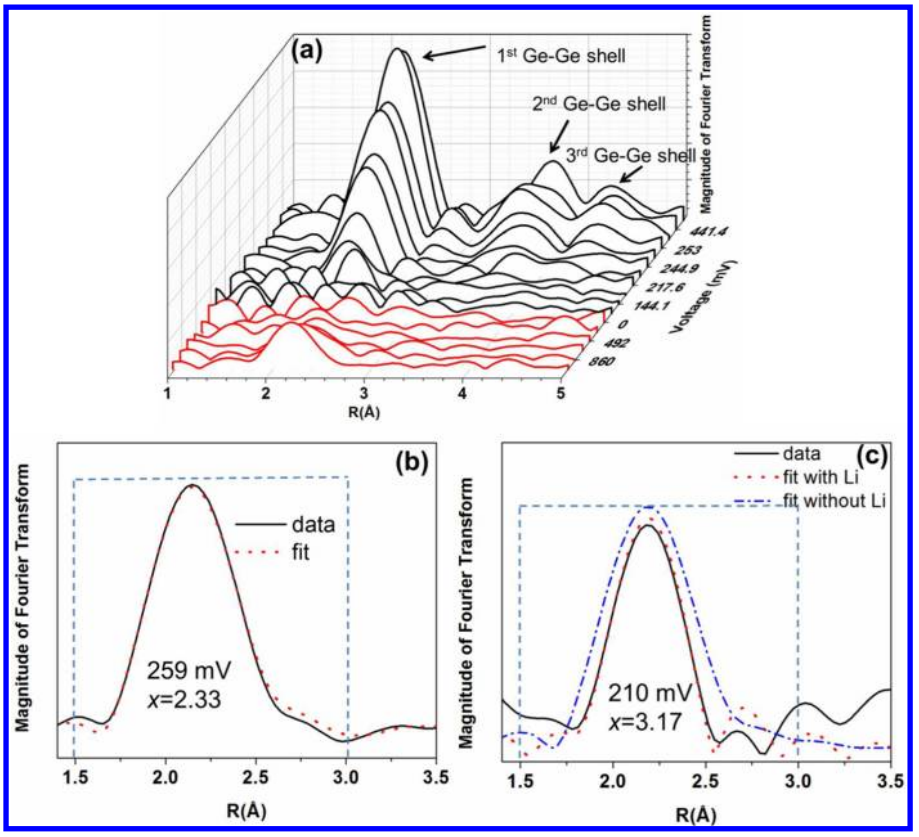

Figure 4. Evolution of (a) Fourier transforms of the Ge K-edge EXAFS spectra during lithiation (black) and delithiation (red), (b) a fit for 259 mV data (x = 2.33) with one Ge−Ge shell, (c) comparison of two fits for 210 mV (x = 3.17) with one Ge−Ge shell (blue dot-dash), and with one Ge−Ge and one Ge−Li shell (red dot).

occurring at ∼255 mV. This indicates a decrease in the concentration of 4p electronic states due to amorphization of Ge and/or phase transformations. The first-derivative of XANES spectra are shown in Figure 3b. The position of the first-derivative peak is related to the average oxidation state of Ge, with a peak at higher energy indicating higher oxidation state. Initially, the oxidation state of Ge remains the same as its pristine state, but the peak starts to shift to lower energy at ∼249 mV (x = 2.53), which becomes more apparent below 241 mV (x = 2.67). The shift of the first-derivative peak to lower energy is due to incorporation of lithium to the Ge lattice forming an a-Li−Ge phase, which provides an electron-shielding effect on the Ge atoms, and hence lowering the energy required to excite the Ge electrons from 1s to 4p states. The onset of the peak energy shift corresponds well with the first electrochemical phase transformation occurring at 253 mV (Figure 2a) and the loss of c-Ge. A more dramatic line shape change in the first-derivative spectra is observed from 144 mV (x = 4.41) to 0 mV (fully lithiated state), where the first-derivative peak becomes much broader. This line shape change coincides well with the second electrochemical phase transformation at ∼151 mV (Figure 2a), where c-$Li_{15}Ge_4$ (and other amorphous phases) are formed.

As lithium is removed, the white-line intensity of the XANES spectra remains broad until the end of delithiation cycle (Figure 3a). Although the line shape of the first-derivative spectra becomes sharper as delithiation proceeds (Figure 3b), the peak position of the first-derivative spectrum at the end of delithiation does not recover to the same peak energy as pristine Ge (Figure 3c). A comparison between the first-derivative spectrum of pristine Ge and the spectrum recorded at the end of delithiation is presented in Figure 3d, showing that the spectrum at the end of delithiation has a lower peak energy compared to the pristine spectrum. The shift in lower energy for the spectrum at the end of delithiation is due to excess negative charges from the dangling bonds in amorphous Ge, and/or the presence of residual lithium bonded to Ge atoms.

The FT of the EXAFS spectra are investigated to better understand the reaction mechanism that occurs during electrochemical cycling (Figure 4a). It can be observed that the intensity of the first, second, and third Ge−Ge shells decreases and disappears as lithiation proceeds. Upon delithiation, only the first Ge−Ge shell intensity partially recovers, and the intensity of the higher-order shells do not recover, which shows that Ge becomes amorphous at the end of the electrochemical cycle. This observation confirms our XRD (Figures 1 and 2) and XANES results (Figure 3), and is due to electrochemically driven solid-state amorphization during lithiation and delithiation of Ge.[26,27] Fitting of the FT of the EXAFS spectra are carried out to investigate the reaction mechanism during lithiation in a more quantitative manner. Briefly, each data set was fitted with a Ge−Ge shell and subsequently a Ge−Li shell was added for data measured below the first phase transformation at ∼253 mV. Figure 4b shows a typical fit using only the Ge−Ge shell for data measured at 259 mV (x = 2.33) and this models the data well. Figure 4c shows a comparison of two fits for 210 mV (x = 3.17), one fit using only a Ge−Ge shell (blue dash-dots), and another using Ge−Ge and Ge−Li shells (red dots). As is apparent, inclusion of the Ge−Li

dx.doi.org/10.1021/cm501233k | Chem. Mater. XXXX, XXX, XXX−XXX

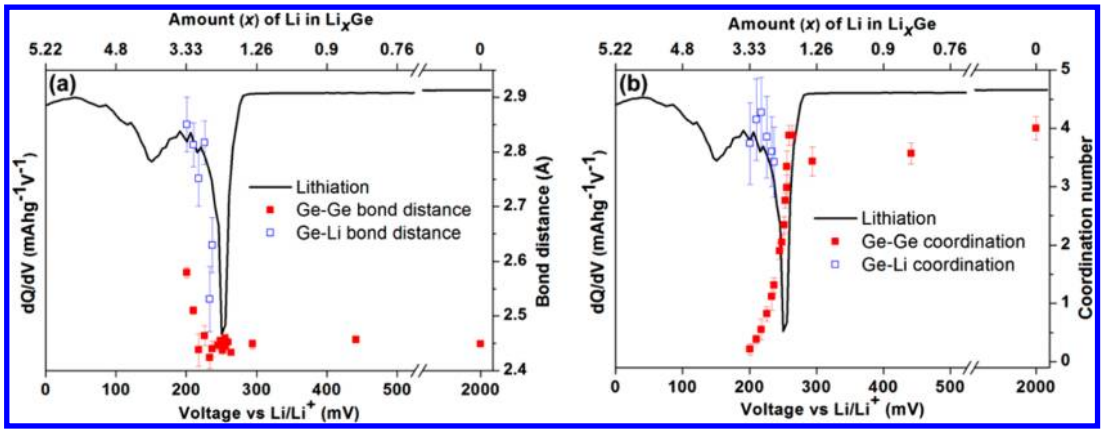

Figure 5. (a) Bond distances and (b) coordination numbers for Ge−Ge bond and Ge−Li bond used in EXAFS fitting. The graphs are overlaid on differential capacity plots for comparison purpose. A magnified version can be found in Figure S4 in the Supporting Information.

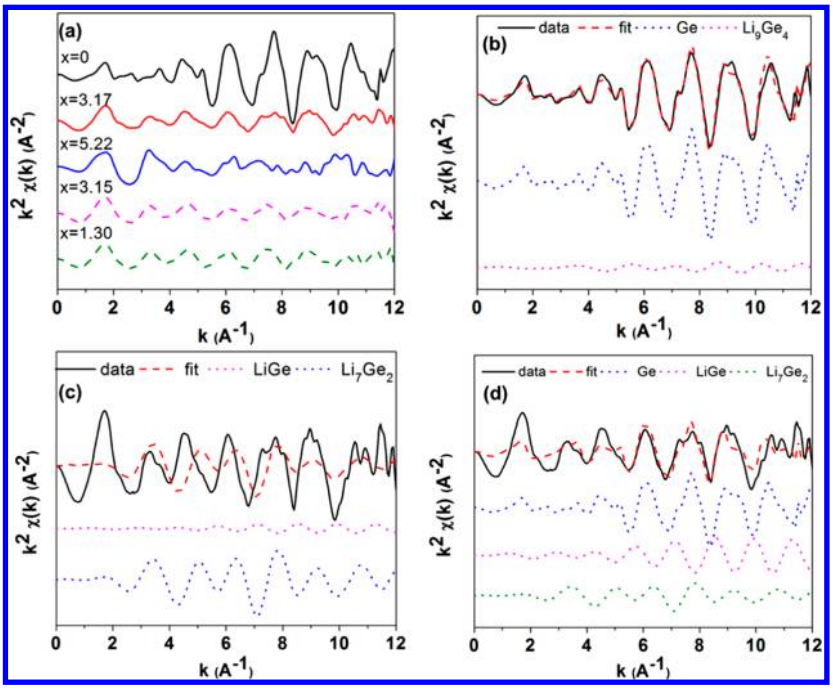

Figure 6. (a) Evolution of *k*-space during lithiation (solid) for 2000 mV (x = 0), 210 mV (x = 3.17) and 0 mV (x = 5.22), and delithiation (dashed) for 596 mV (x = 3.15) and 0 mV (x = 1.30), (b) *k*-space fitting for 253 mV (x = 2.44), (c) *k*-space fitting for 200 mV (x = 3.33) with LiGe and Li_7Ge_2 components, and (d) *k*-space fitting for 200 mV (x = 3.33) with Ge, LiGe, and Li_7Ge_2 components. The fitting range is from k = 3 to 12 $Å^{-1}$.

shell improves the fit significantly. A more statistical representation is presented in Figure S3 in the Supporting Information, where it can be observed that for data measured below 250 mV ($x \geq 2.51$), the inclusion of Ge−Li shell in the fitting improves both *R* factor and reduced chi-square values by at least a factor of 2, showing the necessity of including Li−Ge coordination.

Figure 5a correlates bond distance with differential capacity plotting both versus potential. As lithiation proceeds, the Ge−Ge bond distance stays fairly constant at ∼2.44 Å, corresponding to that of Ge−Ge in diamond-cubic Ge. Even through the first phase transformation peak at 253 mV (x = 2.44), the Ge−Ge bond distances remain largely unchanged. By examining the local interatomic distances of all known Li−Ge phases (see Table S1 in the Supporting Information), Li_9Ge_4 is the only Li−Ge alloy that has a Ge−Ge bond distance similar to that of Ge−Ge in diamond-cubic Ge. This indicates that the a−Li-Ge phase that exists together with c-Ge has similar local atomic environment to that of Li_9Ge_4, herein denoted as a-Li_9Ge_4. Figure 5b shows that there is a rapid decrease in the coordination number as lithiation approaches the first phase transformation peak at 253 mV, due to the phase transformation from Ge to a-Li_9Ge_4, which in the process breaks up Ge−Ge bonds in Ge. This is in good agreement with XRD data in Figure 2a, where there is a rapid decrease in the integrated intensity of Ge.

Below 220 mV (x = 3.02), the Ge−Ge bond distance increases abruptly from 2.44 Å to ∼2.60 Å (Figure 5a), which is similar to the Ge−Ge bond distance of 2.62 Å in Li_7Ge_2, suggesting possible formation of an amorphous phase with an environment similar to a-Li_7Ge_2.

Because of low backscattering intensities of the FT for data measured below 210 mV (x = 3.17) for lithiation and up to 860 mV (x = 2.08) for delithiation, EXAFS fitting on the FTs could not be carried out satisfactorily. Nevertheless, linear combination fitting of the *k*-space EXAFS spectra is carried out to

dx.doi.org/10.1021/cm501233k | *Chem. Mater.* XXXX, XXX, XXX−XXX

elucidate the types of phases that might be present during the different stages of electrochemical cycling in this range. The various possible amorphous Li−Ge phases are calculated by FEFF (Figure S5) and are subsequently employed in linear combination fitting. Details of the FEFF calculations and linear combination fitting procedure can be found in the Supporting Information.

Figure 6a presents the evolution of the *k*-space EXAFS spectra during electrochemical cycling. In the beginning stage, the electrode is still composed of Ge, until about ∼253 mV (x = 2.44), where some presence of a-Li_9Ge_4 are observed together with Ge (Figure 6b). This is supported by EXAFS fitting of the FTs, where the Ge−Ge bond distance agrees well with that of Ge and a-Li_9Ge_4 after the first phase transformation region at ∼253 mV (Figure 5a). Figure 6c shows a poor fit for ∼200 mV (x = 3.33) with LiGe and Li_7Ge_2 components. The inclusion of Ge spectrum in Figure 6d for ∼200 mV (x = 3.33) improves the fit tremendously, indicating the presence of Ge−Ge coordination resembling Ge, even though from XRD results, crystalline-Ge disappears at ∼210 mV (x = 3.17). The persistence of Ge−Ge coordination could be due to the presence of Ge−Ge dumbbells or dimers and other small units in the lithiated state of Ge, as observed for Si.[28] The subsequent formation of a-LiGe (Figure 6d) is possibly due to lithiation of amorphous Ge. Similar observation of the a-LiGe phase during lithiation of amorphous Ge films is also reported in an in situ XAS study,[20] which noted that further lithiation of a-LiGe to form a-Li_7Ge_2.[20] The main difference between our results and the previous in situ XAS work[20] starting with amorphous Ge films is that no a-Li_9Ge_4 was observed in the previous work. We believe that the crystallinity of the Ge electrode impacts the electrochemical reaction that occur during lithiation and delithiation: lithiating c-Ge forms a-Li_9Ge_4 while lithiating a-Ge results in a-LiGe. Note that GeMPs possess higher capacity than Ge thin films, making GeMPs more practical and relevant for rechargeable batteries.

A summary of the phase evolution from XRD and EXAFS analyses is presented in Figure 7. Initially, Ge is 100% crystalline (c-Ge), until ∼1155 mV (Figure 2), where there is a slight drop in c-Ge, attributed to the formation of SEI layer (from the reaction between the Ge electrode and the organic electrolyte), as well as the formation of Li^+ interstitials in Ge. Since no electrochemical lithiation-driven phase transformation has taken place yet, the composition of the electrode is still 100% Ge, comprising c-Ge and a-Ge. As voltage decreases from ∼255 mV, there is a sudden decrease in the Ge fraction. Interestingly, even though c-Ge disappears at ∼210 mV (x = 3.17), Ge is still observed in the *k*-space fitting beyond x = 3.17. This suggests that c-Ge undergoes lithiation inhomogeneously, forming a-Li_9Ge_4 and a-Ge. In particular, at ∼255 mV, all of the a-Li_xGe consisted of a-Li_9Ge_4, and subsequently lithiation leads to the formation of a-Li_7Ge_2 making up the a-Li_xGe composition. At the end of lithiation, the electrode consisted of heterogeneous amorphous phases resembling various Li_xGe phases, and crystalline $Li_{15}Ge_4$ (Figure 7).

Upon delithiation, it is observed that the amount of a-Li_xGe phases increases while the amount of crystalline $Li_{15}Ge_4$ decreases at ∼370 mV ($x \approx 4.91$), showing that crystalline $Li_{15}Ge_4$ is being converted to various amorphous Li_xGe phases. The amount of crystalline $Li_{15}Ge_4$ continues to decrease until it disappears below 492 mV ($x \approx 3.60$), whereas the amount of a-Li_xGe increases. This suggests that crystalline $Li_{15}Ge_4$ does not become amorphous before transforming into other amorphous Li−Ge phases. Finally, the delithiation of a-Li_xGe partly transforms into a-Ge at the end of the electrochemical cycle.

Table 1 presents the EXAFS fitting parameters for the spectrum measured at the end of the first complete cycle, further providing evidence of the existence of Ge−Li coordination, as the fitting improves with the inclusion of Ge−Li shell. The presence of Ge−Li is also supported by Figure 3d, in that the shift in lower energy for the spectrum at the end of delithiation is due to the presence of Li−Ge coordination. We believe that the presence of dangling bonds enhances the attachment of lithium ions to Ge atoms, which contributes to the loss of capacity in this battery system (∼30% capacity loss at the end of delithiation cycle). Additionally, during electrochemical cycling, the volume change associated with insertion and removal of lithium may cause particles become disconnected from the carbon matrix, hindering charge transport and the complete removal of lithium ions during delithiation.

Table 1. Interatomic Distance and Coordination Numbers (CN) for Ge−Ge and Ge−Li Shells Fitted at 2000 mV (end of delithiation)[a]

shell		2000 mV (without Ge−Li)	2000 mV (with Ge−Li)
Ge−Ge	*R* (Å)	2.50 (3)	2.49 (1)
	CN	1.3 (3)	1.0 (1)
Ge−Li	*R* (Å)		2.80 (2)
	CN		4.3 (7)
	R factor	0.222	0.043
	reduced χ^2	209.6	34.8

[a]The fitting result indicates that there are still some Li atoms bonded to Ge atoms at the end of delithiation. Uncertainties in the last digit(s) are given in parentheses.

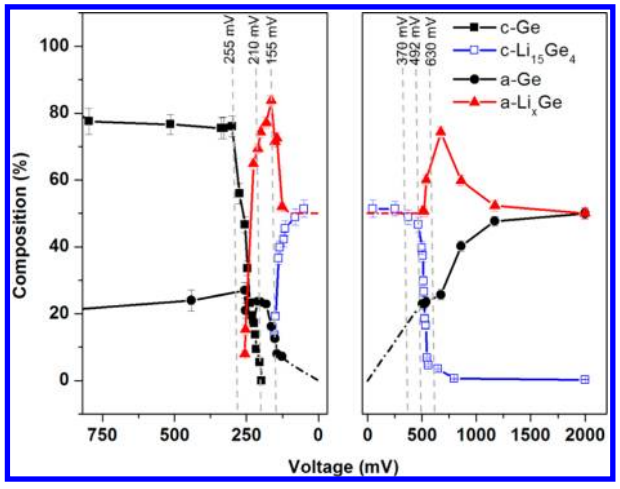

Figure 7. Evolution of various phases during electrochemical cycling of Ge. Here, "c" refers to crystalline, whereas "a" refers to amorphous, and a-Li_xGe consists of Li_9Ge_4, Li_7Ge_2, and LiGe. The dot-dash lines are extrapolation from the trend.

3.3. Reaction mechanism during electrochemical cycling. By correlating XRD, XAS, and electrochemical results, we can now propose a reaction mechanism sequence for the Ge electrode during electrochemical cycling. During lithiation, c-Ge is first converted to a-Li_9Ge_4 at 253 mV (x = 2.44). Subsequent lithiation of c-Ge leads to the formation of a-Ge, followed by heterogeneous a-Li_xGe (consisting of a-Li_9Ge_4, a-

dx.doi.org/10.1021/cm501233k | Chem. Mater. XXXX, XXX, XXX−XXX

LiGe and a-Li_7Ge_2 as evidenced from EXAFS fittings), and in particular, the formation of a-LiGe comes from the lithiation of a-Ge. Then, a-Li_xGe further lithiated to form crystalline $Li_{15}Ge_4$ at 151 mV. During delithiation, the removal of Li^+ from crystalline $Li_{15}Ge_4$ forms a heterogeneous a-Li_xGe, which eventually forms a-Ge. A summary of the proposed reaction steps is expressed as below

$$\text{lithiation: c-Ge} \rightarrow \text{c-Ge} + \text{a-}Li_9Ge_4 \rightarrow \text{a-Ge} + \text{a-}Li_xGe \rightarrow \text{c-}Li_{15}Ge_4$$

$$\text{delithiation: c-}Li_{15}Ge_4 \rightarrow \text{a-}Li_xGe \rightarrow \text{a-Ge}$$

We believe that the peak in the differential capacity plot at 253 mV (Figure 2a) corresponds to the process of crystalline Ge converting to a-Li_9Ge_4. The second peak at 151 mV depicts the formation of crystalline $Li_{15}Ge_4$ from a-Li_xGe. For delithiation, the first peak at 497 mV (Figure 2b) is the conversion of crystalline $Li_{15}Ge_4$ to a-Li_xGe, which is followed by the formation of amorphous Ge from a-Li_xGe at 630 mV.

4. CONCLUSION

In summary, we carried out a combination of in operando XRD and XAS to provide insight into the mechanism of the lithiation process in Ge anodes for LIBs. By correlating XRD and XAS results with electrochemical data, we are able to investigate the various Li−Ge phases that form during electrochemical cycling. In operando XRD provides valuable information on the evolution of crystalline Ge and $Li_{15}Ge_4$, from which we elucidate the crystalline phase transformations that occur during lithiation and delithiation. In operando XAS enables the investigation and identification of possible amorphous Li−Ge phases that are present with the crystalline phases and during the course of the electrochemical cycle. A mechanism is also proposed to help understand the electrochemical reactions that occur during cycling. We found that crystalline Ge lithiates inhomogeneously, first forming amorphous Li_9Ge_4 during the beginning stage of lithiation, followed by the conversion of the remaining crystalline Ge to amorphous Ge. Subsequent lithiation leads to the formation of heterogeneous amorphous phases resembling Li_xGe coordinations, before cystalline $Li_{15}Ge_4$ is formed. During delithiation, $Li_{15}Ge_4$ does not become amorphous before transforming into a-Li_xGe, and eventually forms amorphous Ge. A fundamental understanding of the lithiation and delithiation of Ge can potentially guide us in designing Ge and Ge-based anodes with improved performance. Both our in operando XRD and XAS results present new insights into the reaction mechanism of Ge as anodes in LIBs, and demonstrate the importance of correlating electrochemical results with in operando studies.

■ ASSOCIATED CONTENT

Ⓢ Supporting Information

Additional figures and table, determination of crystalline phase fractions, and procedure information. This material is available free of charge via the Internet at http://pubs.acs.org.

■ AUTHOR INFORMATION

Corresponding Author

*E-mail: mftoney@slac.stanford.edu.

Notes

The authors declare no competing financial interest.

■ ACKNOWLEDGMENTS

Portions of this research were carried out at the Stanford Synchrotron Radiation Lightsource, a Directorate of SLAC National Accelerator Laboratory and an Office of Science User Facility operated for the U.S. Department of Energy Office of Science by Stanford University.

■ REFERENCES

(1) Armand, M.; Tarascon, J.-M. *Nature* **2008**, *451*, 652−657.
(2) Bruce, P. G.; Scrosati, B.; Tarascon, J.-M. *Angew. Chem., Int. Ed.* **2008**, *47*, 2930.
(3) Cabana, J.; Monconduit, L.; Larcher, D.; Palacín, M. R. *Adv. Mater.* **2010**, *22*, E170.
(4) Hayner, C. M.; Zhao, X.; Kung, H. H. *Annu. Rev. Chem. Biomol. Eng.* **2012**, *3*, 445.
(5) Shukla, A. K.; Kumar, T. P. *J. Phys. Chem. Lett.* **2013**, *4*, 551.
(6) Scrosati, B.; Hassoun, J.; Sun, Y.-K. *Energy Environ. Sci.* **2011**, *4*, 3287.
(7) Etacheri, V.; Marom, R.; Elazari, R.; Salitra, G.; Aurbach, D. *Energy Environ. Sci.* **2011**, *4*, 3243.
(8) Park, C.-M.; Kim, J.-H.; Kim, H.; Sohn, H.-J. *Chem. Soc. Rev.* **2010**, *39*, 3115.
(9) Fuller, C. S.; Severiens, J. C. *Phys. Rev.* **1957**, *96*, 21.
(10) Wang, D.; Chang, Y.-L.; Wang, Q.; Cao, J.; Farmer, D. B.; Gordon, R. G.; Dai, H. *J. Am. Chem. Soc.* **2004**, *126*, 11602.
(11) Chan, C. K.; Peng, H.; Liu, G.; McIlwrath, K.; Zhang, X. F.; Huggins, R. A.; Cui, Y. *Nat. Nanotechnol.* **2007**, *3*, 31.
(12) Ren, J.-G.; Wu, Q.-H.; Tang, H.; Hong, G.; Zhang, W.; Lee, S.-T. *J. Mater. Chem. A* **2013**, *1*, 1821.
(13) Kim, M. G.; Cho, J. *J. Electrochem. Soc.* **2009**, *156*, A277.
(14) Seng, K. H.; Park, M.-H.; Guo, Z. P.; Liu, H. K.; Cho, J. *Angew. Chem., Int. Ed.* **2012**, *51*, 5657.
(15) Lee, H.; Kim, M. G.; Choi, C. H.; Sun, Y. K.; Yoon, C. S.; Cho, J. *J. Phys. Chem. B* **2005**, *109*, 20719.
(16) Fan, S.; Lim, L. Y.; Tay, Y. Y.; Pramana, S. S.; Rui, X.; Samani, M. K.; Yan, Q.; Tay, B. K.; Toney, M. F.; Hng, H. H. *J. Mater. Chem. A* **2013**, *1*, 14577.
(17) Graetz, J.; Ahn, C. C.; Yazami, R.; Fultz, B. *J. Electrochem. Soc.* **2004**, *151*, A698.
(18) Yoon, S.; Park, C.-M.; Sohn, H.-J. *Electrochem. Solid-State Lett.* **2008**, *11*, A42.
(19) Baggetto, L.; Notten, P. H. L. *J. Electrochem. Soc.* **2009**, *156*, A169.
(20) Baggetto, L.; Hensen, E. J. M.; Notten, P. H. L. *Electrochim. Acta* **2010**, *55*, 7074.
(21) Chan, C. K.; Zhang, X. F.; Cui, Y. *Nano Lett.* **2008**, *8*, 307.
(22) Nelson, J.; Misra, S.; Yang, Y.; Jackson, A.; Liu, Y.; Wang, H.; Dai, H.; Andrews, J. C.; Cui, Y.; Toney, M. F. *J. Am. Chem. Soc.* **2012**, *134*, 6337.
(23) Misra, S.; Liu, N.; Nelson, J.; Hong, S. S.; Cui, Y.; Toney, M. F. *ACS Nano* **2012**, *6*, 5465.
(24) Mannsfeld, S. *wxdiff: Diffraction image processing and data analysis software* 2010, http://code.google.com/p/wxdiff/.
(25) Ravel, B.; Newville, M. *J. Synchrotron Radiat.* **2005**, *12*, 537.
(26) Limthongkul, P.; J, Y.-I.; Dudney, N. J.; Chiang, Y.-M. *J. Power Sources* **2003**, *119−121*, 604.
(27) Limthongkul, P.; J, Y.-I.; Dudney, N. J.; Chiang, Yet-M. *Acta Mater.* **2003**, *51*, 1103.
(28) Key, B.; Morcrette, M.; Tarascon, J.-M.; Grey, C. P. *J. Am. Chem. Soc.* **2011**, *133*, 503.